CLICdp-Draft-20xx-xxx
14 March 2018

In situ detector calibration at CLIC.

J-J. Blaising [‡], D. Dannheim [†], A. Sailer [†]

On behalf of the CLICdp Collaboration

[*] *CERN, Switzerland,* [‡] *Laboratoire d'Annecy-le-Vieux de Physique des Particules, Annecy-le-Vieux, France*

Abstract

CLIC is proposed to run according to a staging scenario with centre-of-mass energies increasing from $\sqrt{s} = 380$ GeV to 3 TeV. Achieving good physics performance requires accurate alignment and calibration of the detector as well as regular monitoring of the alignment and calibration prarameters. During physics runs this is achieved using particles from $ee, e\gamma$ and $\gamma\gamma$ interactions. Standard Model cross sections depend on the centre-of-mass energy. As a result, processes relevant for calibration are different at the various energies. This note discusses the main detector calibration topics at two different centre-of-mass energies of CLIC, $\sqrt{s} =$ 380-350 GeV and 1.4 TeV. It estimates the total and differential muon rates available for the detector alignment as well as the performance reachable for the momentum scale and total energy scale calibration. For the first stage of CLIC special calibration runs at $\sqrt{s} = 91$ GeV are also considered. After the first year of running the high muon rate allows an accurate alignment and a regular control of the alignment parameters. $Z \to \mu^+\mu^-$ and $K^0_s \to \pi^+\pi^-$ events allow a good control of the momentum resolution and an accurate determination of the global and differential momentum scale. At $\sqrt{s}$=91.2 GeV the di-muon event sample provides a direct measurement of the momentum resolution and an accurate determination of the momentum scale. The di-jet event sample allows a direct measurement of the di-jet energy resolution and an accurate determination of the di-jet energy scale. It allows also the flavour tagging efficiency measurement At the lowest centre-of-mass energy a measurement of the top mass will be done measuring the top production cross section in the energy range $\sqrt{s} = 340$ GeV to 350 GeV. This note presents also the method to measure the absolute centre-of-mass energy and the accuracy reachable for the top threshold scan.

This work was carried out in the framework of the CLICdp Collaboration

1 Introduction

CLIC is proposed to run according to a staging scenario with different centre-of-mass energies. For this study a scenario with stages at $\sqrt{s} = 380$-350 GeV, 1.5 TeV and 3 TeV is assumed. To reach good physics performance at each centre-of-mass energy requires accurate alignment and calibration of the detector as well as regular monitoring of the alignment and calibration parameters. The main calibration issues to address are:

- Muon and tracker system alignment
- Detection and particle identification efficiency
- Charged particle momentum resolution and momentum scale calibration
- Calorimeter calibration, ECAL, HCAL, LCAL, BCAL
- Jet energy resolution and scale calibration
- Missing *Et* resolution and scale calibration
- Flavour tagging performance

Prior to the detector assembly single and combined detector calibration will be performed in beam tests. Accurate detector alignment can only be done after detector assembly. After alignment the charged particle momentum resolution can be measured and compared with the resolution of Monte Carlo events; the absolute momentum scale can be determined using the invariant mass of well known particles, e.g M_Z and $M_{K_s^0}$. Once the momentum scale is known, the ECAL and HCAL calibration can be done using electrons and isolated charged hadrons by comparing the energy deposition in the calorimeters with the track momentum. Once the ECAL and HCAL calibration parameters are set the energy resolution can be measured and the total energy scale can be determined using di-jet events originating from Z or W bosons.

The main contributions to the di-jet energy resolution are:

- Tracking efficiency
- Momentum resolution
- Calorimeter energy resolution
- Leakage
- Particle confusion
- Jet confusion

These contributions change with the centre-of-mass energy. At each energy the data-Monte Carlo comparison of the di-jet invariant mass is needed to determine the di-jet energy resolution and the energy scale. At the lowest centre-of-mass energy a measurement of the top mass will be done measuring the top production cross section in the energy range $\sqrt{s} = 340$ GeV to 350 GeV. This note describes also the method to measure the absolute centre-of-mass energy and the centre-of-mass energy accuracy reachable for the top threshold scan.

2 Luminosities at CLIC

Table 1 lists the expected nominal luminosities at CLIC at the three centre-of-mass energies $\sqrt{s} = 350$ GeV, 1.5 TeV and 3 TeV. At each centre-of-mass energy the luminosity yield is reduced the first three years; the scaling factor is 5%, 25% and 50% for year-1, year-2 and year-3 respectively [1]. The table shows also the expected luminosity at $\sqrt{s} = 91.2$ GeV. At the Z energy the luminosity with respect to the luminosity at $\sqrt{s} = 350$ GeV is reduced by a factor 64 [2]. Table 1 shows also the expected luminosities per day in the first two years.

Table 1: Expected luminosities at CLIC

$\sqrt{s}$ GeV	Luminosity [$cm^{-2}s^{-1}$]	Luminosity [$cm^{-2}s^{-1}$] Year-1	Luminosity/day [pb^{-1}]	Luminosity/day [pb^{-1}] Year-1	Luminosity/day [pb^{-1}] Year-2
380	1.5×10^{34}	7.5×10^{32}	1300	65	325
1400	3.7×10^{34}	1.8×10^{33}	3200	160	800
3000	5.9×10^{34}	2.9×10^{33}	5100	255	1275
91	2.3×10^{32}	1.2×10^{31}	20	1	5

At LEP1 the peak luminosity was L_0=$3.4\times10^{30} cm^{-2}s^{-1}$; table 2 shows the LEP luminosities in 1994 and 1995 [3]. At CLIC at $\sqrt{s} = 91$ GeV despite a reduction of the luminosity the integrated luminosity

Table 2: LEP luminosities in 1994 and 1995.

Year	Beam energy [GeV]	Total Luminosity [pb^{-1}]	Average Luminosity [pb^{-1}/day]
1994	45.6	64	0.31
1995	45.6 - 70.0	47	0.23

per day could be significant; it is therefore worthwhile to study the calibration potential at $\sqrt{s} = 91$ GeV.

3 Fast Event Simulation

The WHIZARD program [4] was used to compute the cross sections and generate the events of the various processes considered for the detector calibration. The luminosity spectrum is generated using GUINEAPIG [5]; it is interfaced to WHIZARD using Circe2 [4]. The effects of Initial State Radiation (ISR) are also included in WHIZARD. Quark fragmentation and hadronization is performed using the PYTHIA program [6]. For the leptons the default PYTHIA treatment of Final State Radiation (FSR) is used. At $\sqrt{s}$=91 GeV no luminosity spectrum has been generated; only ISR contributes to the luminosity spectrum. To take into account the detector resolution, the momentum and energy of the particles are randomly modified using different gaussian resolution parameters according to the particle type.

- Charged particle momentum resolution function

$$\frac{\sigma(P)}{P} \approx a \cdot P \oplus b \cdot \frac{1}{\sqrt{sin\theta}} \oplus c \cdot \frac{cos\theta}{sin\theta} \tag{1}$$

  Parameter a, b and c represents the contribution from the curvature measurement, from the multiple-scattering and from the angular resolution respectively.

$$a = \frac{\sigma_{r\phi}\sqrt{K/(N+4)}}{0.3BL^2} \tag{2}$$

B [Tesla] is the magnetic field value, L [m] the track length, N the number of measurement points and K=720. For $\theta = 90^\circ$ $a = 2.0 \times 10^{-5}$, $b = 2.0 \times 10^{-3}$ and $c = 2.0 \times 10^{-4}$
For tracks measured in the tracker barrel; $\theta > 40^\circ$ and $\theta < 140^\circ$ parameter a is indepent of θ. For tracks measured in the end cap disks the path length L depends on θ and therefore a depends on θ

$$a_\theta = a \times \left(\frac{tan\theta_{40}}{\tan\theta}\right)^2 \tag{3}$$

- Photon energy resolution function

$$\frac{\sigma(E)}{E} = 0.15/\sqrt{E}\ [GeV] \tag{4}$$

- Neutral hadron energy resolution function

$$\frac{\sigma(E)}{E} = 0.55/\sqrt{E}\ [GeV] \tag{5}$$

In the introduction the main contributions to the total energy resolution are listed. Several of them cannot be approximated in a fast simulation; e.g. leakage, particle confusion. This leads to an underestimation of the total energy resolution. To make the fast simulation more realistic the following assumptions have been included.

- track efficiency 99%
- No charged particle identification; mass of charged hadron = pion mass
- No neutral particle identification; mass of neutral hadron = kaon mass

The Fastjet exclusive *kt* algorithm [7] is used for jet clustering.

4 Fractional Luminosities

CLIC is not only an e^+e^- collider, it also collides photons and electrons (positrons) with photons. The instantaneous luminosity of these collisions are not the same and for a given time frame, the integrated luminosities are different. Table 3 shows the instantaneous luminosities normalised to the e^+e^- luminosity for different centre-of-mass energies. To estimate the particle production rates these luminosity correction factors are taken into account.

Table 3: Luminosity correction factors

$\sqrt{s} =$		350 GeV	1400 GeV	3000 GeV
Interaction	Luminosity correction			
e^+e^-		1	1	1
$e^-\gamma$	L($e^-\gamma$)/ L(e^+e^-)	0.45	0.75	0.79
$e^+\gamma$	L($e^+\gamma$)/ L(e^+e^-)	0.45	0.75	0.79
$\gamma\gamma$	L($\gamma\gamma$)/ L(e^+e^-)	0.23	0.64	0.69

5 Detector Alignment and Calibration at $\sqrt{s}$=350 GeV

Table 4 shows the cross sections of the main muon final processes processes at $\sqrt{s}$ = 350 GeV. The cross section calculation and event generation was done for muons with $E_{\mu^\pm} > 5$ GeV and $10^\circ < \theta_\mu < 170^\circ$. The table shows also the number of events assuming an integrated luminosity of 1 fb^{-1} and taking into account the luminosity factors. For an integrated luminosity of 1 fb^{-1} the total number of muons produced is about 5×10^5.

Table 4: Cross sections of $e^+e^-, e^-\gamma$ and $\gamma\gamma$ interactions with muon final states; $\sqrt{s}$ = 350 GeV

Process	σ [fb] $E_{\mu^\pm} > 5$ GeV; $10^\circ < \theta_\mu < 170^\circ$	Luminosity factor	Events/fb^{-1}
$e^+e^- \to \mu^+\mu^-(\gamma)$	2.0×10^3	1	2.0×10^3
$e^+e^- \to e^-\bar{\nu}_e\mu^+\nu_\mu(\times 2)$	1.0×10^5	1	2.0×10^5
$e^+e^- \to e^+e^-\mu^+\mu^-$	3.0×10^4	1	3.0×10^4
$e^-\gamma \to \mu^+\mu^-e^- \quad (\times 2)$	2.8×10^5	0.45	1.3×10^5
$\gamma\gamma \to \mu^+\mu^-$	6.4×10^5	0.23	1.5×10^5
All			4.7×10^5

Table 5 shows the cross sections for di-jet final state processes at $\sqrt{s}$ = 350 GeV. It shows also the number of hadronic final state events assuming an integrated luminosity of 1 fb^{-1} and taking into account the luminosity factors.

Table 5: Cross sections of $e^+e^-, e^-\gamma$ and $\gamma\gamma$ interactions with di-jet final states

Process	σ [fb] $E_q > 10$ GeV; $10^\circ < \theta_q < 170^\circ$	Luminosity factor	Events/fb^{-1}
$e^+e^- \to q\bar{q}(\gamma)$	1.7×10^4	1	1.7×10^4
$e^+e^- \to e^+e^-q\bar{q}$	1.8×10^3	1	1.8×10^3
$e^+e^- \to e^-\nu q\bar{q}$	1.2×10^3	1	1.2×10^3
$e^-\gamma \to \nu q\bar{q}(\times 2)$	1.1×10^3	0.45	5.0×10^2
$e^-\gamma \to e^-q\bar{q}(\times 2)$	8.0×10^4	0.45	3.6×10^4

5.1 Tracker Alignment

Tracking systems alignment requires a large number of tracks. The alignment of the CMS tracker for the first high-luminosity data-taking period during the year 2011 was done using tracks from several data sets; isolated muons originating from leptonic W decays, tracks from minimum bias events, muons from Z-boson decays and cosmic ray tracks. The total number of tracks was about 20×10^6 [8].

Figure 1(a) shows the muon momentum distribution of the processes listed in Table 4. The momentum of the muons extends over a large range and is adequate for the tracking systems alignment. Figure 1(b) shows the angular distribution of the muons. The plots show the distributions corresponding to an integrated luminosity of $1 fb^{-1}$. The number of tracks in the central region is about 5×10^3 per bin of 1°; it is significantly higher in the forward region. The muon rate is about 800000 tracks per fb^{-1} providing a total rate of about 4×10^6 muon tracks at the end of the first year and 20×10^6 at the end of the second year.

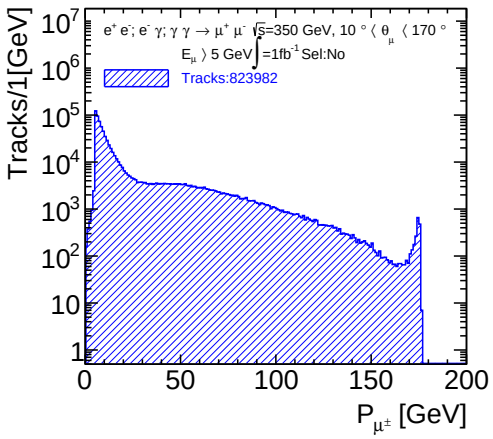

(a) muon momentum distribution

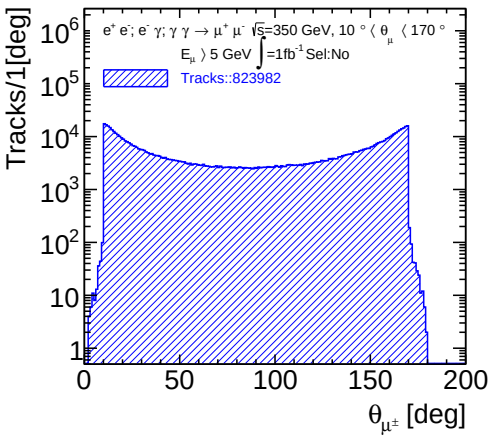

(b) muon angular distribution

Figure 1: $e^+e^-, e^-\gamma$ and $\gamma\gamma$ interactions with muon final states at $\sqrt{s}$=350 GeV (a) muon momentum distribution (b) muon angular distribution

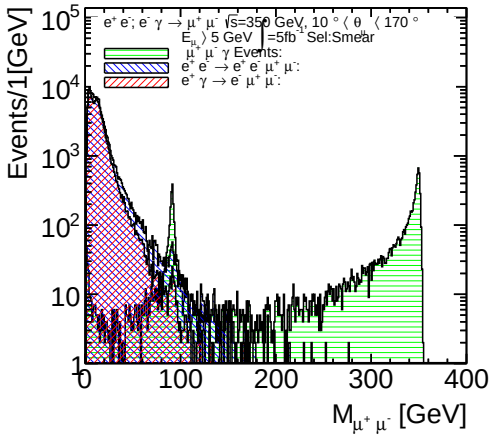

(a) Invariant di-muon mass spectrum

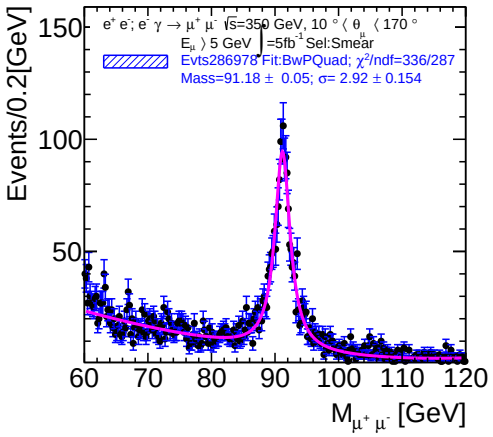

(b) Fit of the invariant mass spectrum

Figure 2: $e^+e^-; e^-\gamma \to \mu^+\mu^-$ at $\sqrt{s}$=350 GeV with momentum smearing (a) Invariant di-muon mass spectrum (b) Fit of the invariant mass spectrum

5.2 Momentum Resolution and Momentum Scale Calibration

Figure 2(a) shows the muon invariant mass of the processes e^+e^- and $e^-\gamma \to \mu^+\mu^-$ at $\sqrt{s}$=350 GeV. The number of events in the plot correspond to an integrated luminosity of $5\,\text{fb}^{-1}$. The momentum of the muons was smeared using the charged particle momentum resolution given in section 3; the Z peak is clearly visible. Figure 2(b) shows the fit of the muon invariant mass in the Z region. M_Z=91.18 $\pm$ 0.05 GeV $\Gamma(M_Z)$=2.92 $\pm$ 0.15 GeV. The global momentum scale can be determined with a relative uncertainty $\sigma(M_Z)/M_Z$=5×10^{-4}. With more luminosity the momentum scale as a function of the angle can be determined.

The charged particle momentum scale can also be determined measuring the $\pi^+\pi^-$ invariant mass of $K_s^0 \to \pi^+\pi^-$ events. K_s^0 particles are produced in $e^+e^- \to \tau^+\tau^-$ interactions and in all processes with hadronic final states. The following plots illustrate the potential of momentum scale measure-

ment using K_s^0 decays in hadronic events. Figure 3(a) shows the hadron momentum distribution of the charged hadrons in the process $e^+e^-;e^-\gamma \to q\bar{q}$. Figure 3(b) shows the fit of the $\pi^+\pi^-$ invariant mass in the K_s^0 region. The number of events in the plots correspond to an integrated luminosity of 1 fb^{-1}. $M_{K_s^0}$=0.4977 $\pm$ 2 $\times$ 10^{-5} GeV; the global momentum scale can be determined with a relative uncertainty $\delta(M_{K_s^0})/M_{K_s^0}$=4 $\times$ 10^{-5}.

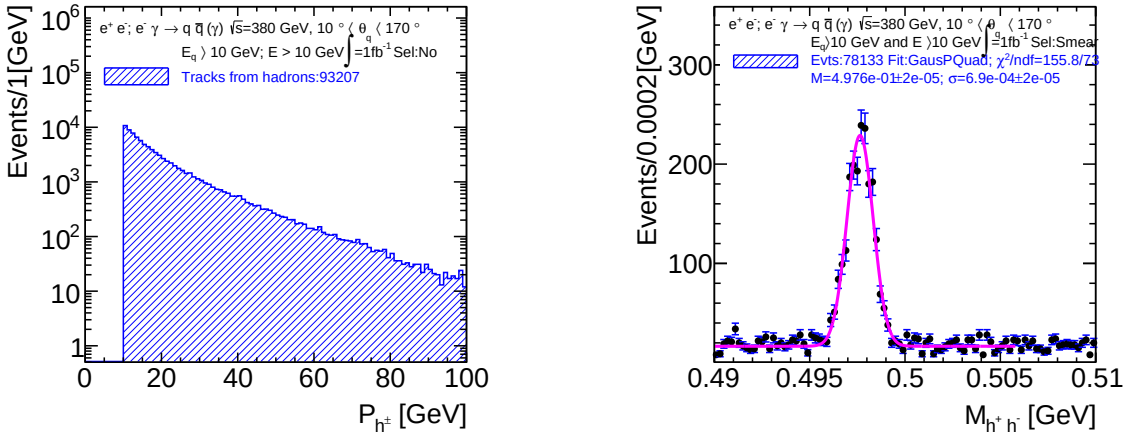

(a) h^+h^- momentum distribution

(b) h^+h^- invariant mass scpectrum fit

Figure 3: $e^+e^-;e^-\gamma \to q\bar{q}(\gamma)$ at $\sqrt{s}$=350 GeV (a) h^+h^- momentum distribution (b) h^+h^- invariant mass scpectrum fit

At $\sqrt{s}$=350 GeV, $Z \to \mu^+\mu^-$ and $K_s^0 \to \pi^+\pi^-$ events allow a good control of the momentum resolution and an accurate determination of the global and differential momentum scale.

5.3 Di-jet Energy Resolution and Energy Scale

Figure 4(a) shows the correlation between the di-quark invariant mass and the angle between the quarks for the processes $e^+e^-;e^-\gamma \to q\bar{q}\gamma$ at $\sqrt{s}$=350 GeV. Most Z events have a di-quark angle around 60°; for W's the angle ranges from 50° to 70°. Figure 4(b) shows the di-quark invariant mass; Z events are clearly visible; a smaller W peak is also visible. Figure 5(a) shows the di-jet invariant mass after quark fragmentation and hadronization and without particle energy smearing; the Fastjet exclusive *kt* algorithm is used for jet clustering. The Z peak broadening is only due to the jet confusion created by the small angle between the jets. Figure 5(b) shows the di-jet invariant mass after quark fragmentation and hadronization and with particle energy smearing. The particle energy smearing does not significantly increase the Z width. Figure 6(a)shows the fit of di-jet invariant mass, with particle smearing, in the Z region. The fit function is a Breit-wigner function for the peak and argus function for the background. Around 80 GeV one may guess the presence of W events but there is no W, Z mass separation. The fit result is M_Z=88.59 $\pm$ 0.30 GeV and Γ_Z=18.1 GeV. Figure 6(b) shows the di-jet invariant mass fit excluding W events produced by the processes $e^+e^- \to e^-\nu q\bar{q}$ and $e^-\gamma \to e^-\nu q\bar{q}$. The fit result is M_Z=89.93 $\pm$ 0.13 GeV and Γ_Z=11.12 GeV; the mass value is closer to the Z mass; unfortunately in real data one cannot discard the W events. At $\sqrt{s}$=350 GeV the di-jet mass resolution is poor and doesn't allow an accurate determination of the di-jet energy scale. The contamination of Z events by W's leads to a data sample requiring Monte Carlo corrections for heavy flavour tagging efficiency measurement. Heavy flavour tagging efficiency measurement can also be done using the process $e^+e^- \to ZZ \to l^+l^-q\bar{q}$. The event selection requires di-muon or di-electron events compatible with a Z mass; it is only after the second year that the event rate is large enough to measure heavy flavour tagging efficiency.

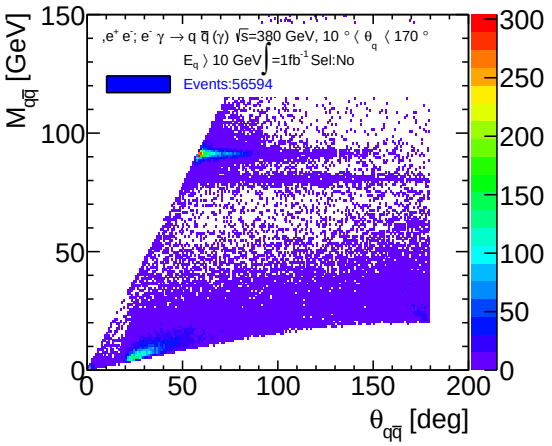

(a) Correlation between the di-quark invariant mass and the angle between the quarks

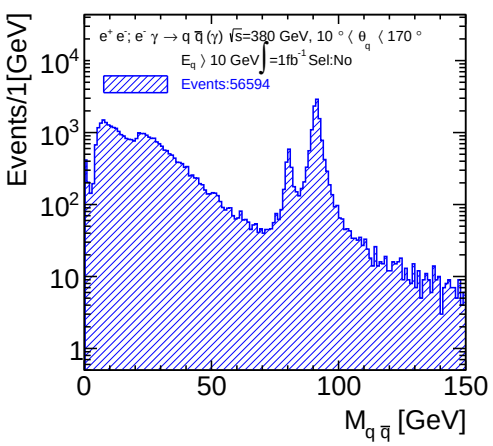

(b) di-quark invariant mass distribution

Figure 4: $e^+e^-; e^-\gamma \to q\bar{q}(\gamma)$ at $\sqrt{s}$=350 GeV (a) Correlation between the di-quark invariant mass and the angle between the quarks (b) di-quark invariant mass distribution

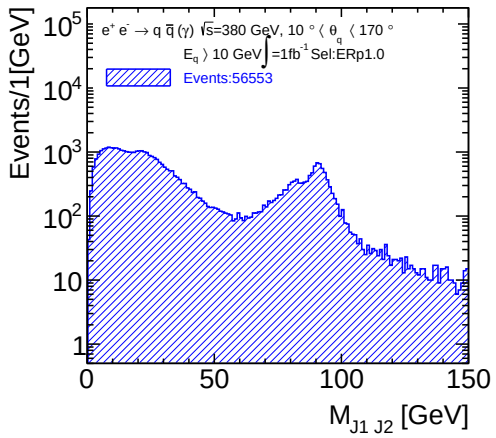

(a) di-jet invariant mass after jet clustering and without particle energy smearing

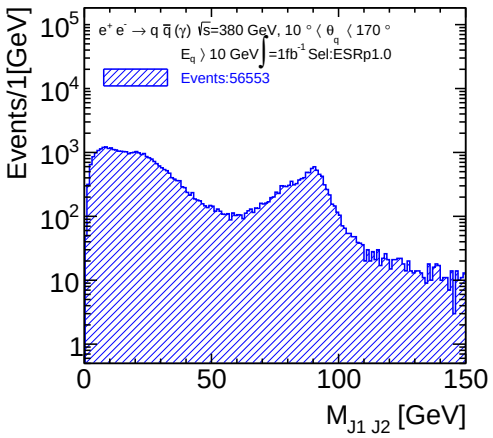

(b) di-jet invariant mass after jet clustering and with particle energy smearing

Figure 5: $e^+e^-; e^-\gamma \to q\bar{q}(\gamma)$ at $\sqrt{s}$=350 GeV (a) di-jet invariant mass after jet clustering and without particle energy smearing (b) di-jet invariant mass after jet clustering and with particle energy smearing

5.4 Absolute Centre-of-mass Energy Determination

At the lowest centre-of-mass energy a measurement of the top mass will be done measuring the top production cross section for ten different centre-of-mass values in the energy range from $\sqrt{s} = 340$ GeV to 350 GeV. An integrated luminosity of $10 fb^{-1}$ will be used for each cross section measurement The statistical accuracy of top mass mass measurement is 27 MeV for the nominal luminosty spectrum. To estimate the systematic error it is necessary to know the accuracy on the centre-of-mass energy. The measurement of the centre-of-mass energy can be done using $e^+e^- \to \mu^+\mu^-(\gamma)$ events. In absence of initial state radiation the centre-of-mass energy is $\sqrt{s} = E_{\mu^+} + E_{\mu^-}$. In presence of initial state radiation

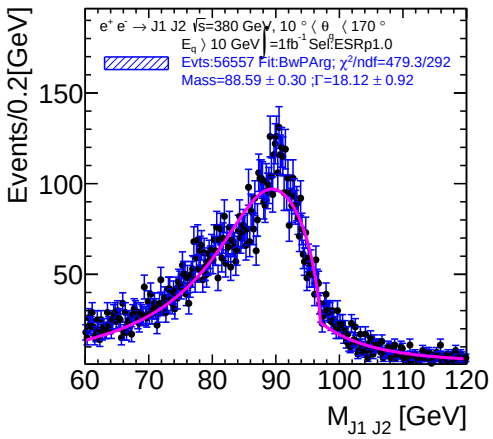

(a) di-jet invariant mass spectrum; all events

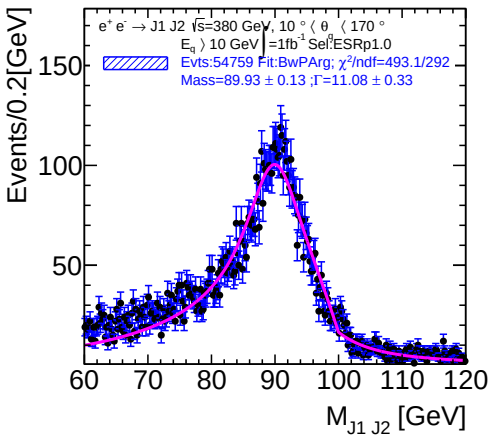

(b) di-jet invariant mass spectrum; no W contribution

Figure 6: $e^+e^-;e^-\gamma \to q\bar{q}(\gamma)$ at $\sqrt{s}$=350 GeV (a) di-jet invariant mass spectrum fit; all events (b) di-jet invariant mass spectrum fit; no W contribution

the momentum of the photon can be infered using the momentum of the di-muon system and sqrts is detemined using the following relation.

$$\sqrt{s} = E_{\mu^+} + E_{\mu^-} + |\overrightarrow{P_{\mu^+}} + \overrightarrow{P_{\mu^-}}| \tag{6}$$

Figure 7(a) shows the reconstructed $\sqrt{s}$ distribution obtained using formula 6. Figure 7(b) shows the di-muon invariant mass distribution. To reduce the $e^+e^-\mu^+\mu^-$ and $e^-\mu^+\mu^-$ backgrounds which extend into the $\sqrt{s}$ peak distribution a cut on the invariant mass is applied.

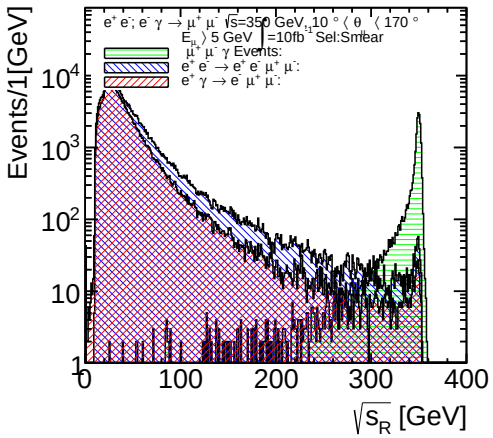

(a) Reconstructed $\sqrt{s}$ distributions

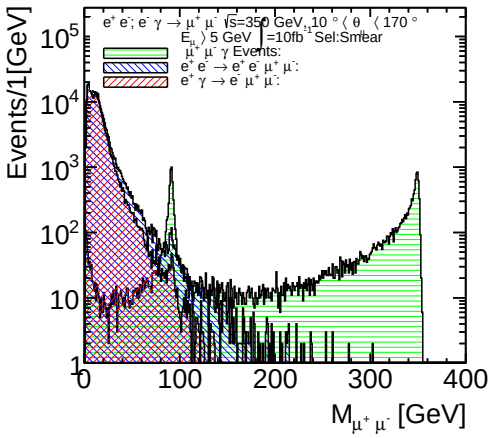

(b) Di-muon invariant mass distributions

Figure 7: $e^+e^- \to \mu^+\mu^-(\gamma)$ at $\sqrt{s}$=350 GeV (a) Reconstructed $\sqrt{s}$ distributions (b) Di-muon invariant mass distributions

Figure 8(a) shows the reconstructed $\sqrt{s}$ distribution selecting events with a di-muon invariant mass greater than 300 GeV. The background is strongly suppressed. Figure 8(b) shows the fit of the reconstructed $\sqrt{s}$ distribution for events with a di-muon invariant mass greater than 300 GeV; $\sqrt{s}$=349.91

$\pm$ 0.03 GeV. At $\sqrt{s}$=380 GeV for an integrated luminosity of 100 fb^{-1} $\sqrt{s}$ can be determined with an accuracy lower than 10 MeV.

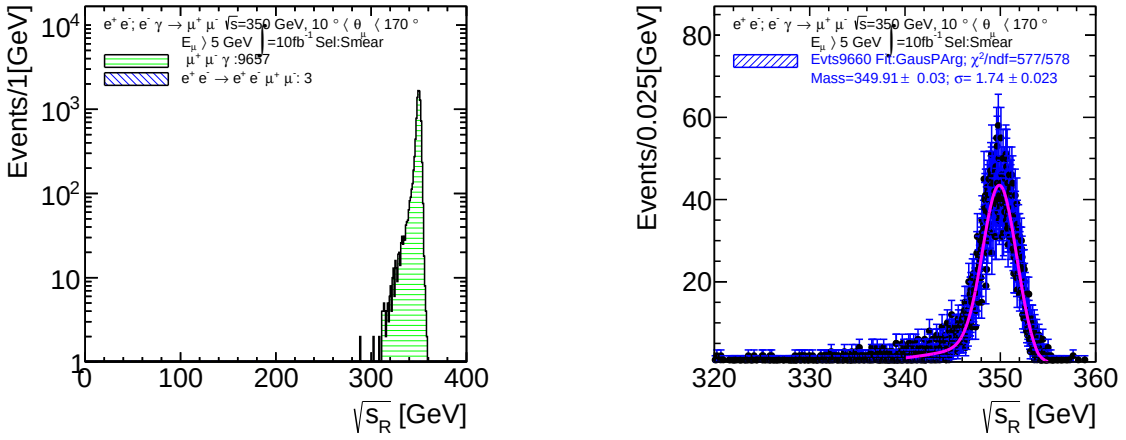

(a) Reconstructed $\sqrt{s}$ distributions

(b) Fit of the reconstructed $\sqrt{s}$ distributions

Figure 8: $e^+e^- \to \mu^+\mu^-(\gamma)$ at $\sqrt{s}$=350 GeV (a) Reconstructed $\sqrt{s}$ distributions (b) Fit of the reconstructed $\sqrt{s}$ distributions

6 Detector Alignment and Calibration at $\sqrt{s}$=1400 GeV

Table 6 shows the cross sections for muon final processes at $\sqrt{s}$ = 1400 GeV; it shows also the expected number of events assuming an integrated luminosity of 1 fb^{-1} and taking into account the luminosity factors. In the first year it will take about 6 days to reach an integrated luminosity of 1 fb^{-1}. Table 7

Table 6: Cross sections of $e^+e^-, e^-\gamma$ and $\gamma\gamma$ interactions with muon final states at $\sqrt{s}$ = 1400 GeV.

Process	σ [fb] $E_{\mu^\pm} > 5$ GeV; $10^\circ < \theta_\mu < 170^\circ$	Luminosity factor	Events/fb^{-1}
$e^+e^- \to \mu^+\mu^-\gamma$	2.0×10^2	1	2.0×10^2
$e^+e^- \to e^-\bar{\nu}_e\mu^+\nu_\mu(\times2)$	6.5×10^5	1	6.5×10^5
$e^+e^- \to e^+e^-\mu^+\mu^-$	3.8×10^4	1	3.8×10^4
$e^-\gamma \to \mu^+\mu^-e^-(\times2)$	2.4×10^5	0.75	1.8×10^5
$\gamma\gamma \to \mu^+\mu^-$	3.4×10^5	0.64	2.2×10^5
All			1.2×10^6
hline			

shows the cross sections for di-jet final state processes at $\sqrt{s}$ = 1400 GeV. It shows also the number of expected hadronic final state events assuming an integrated luminosity of 1 fb^{-1} and taking into account the luminosity factors.

6.1 Tracker Alignment

Figure 9(a) shows the momentum distribution of the muons of the processes listed in Table 6. The number of events corresponds to an integrated luminosity of 1 fb$^-$1. The total track rate is about 1.4×10^6

Table 7: Cross sections of $e^+e^-, e^-\gamma$ and $\gamma\gamma$ interactions with di-jet final states at $\sqrt{s}$ = 1400 GeV.

Process	σ [fb] $E_q > 10$ GeV; $10^\circ < \theta_q < 170^\circ$	Luminosity factor	Events/fb^{-1}
$e^+e^- \to q\bar{q}\gamma$	1.2×10^3	1	1.2×10^3
$e^+e^- \to e^+e^- q\bar{q}\gamma$	1.2×10^4	1	1.2×10^4
$e^+e^- \to e^+\nu q\bar{q}\gamma(\times 2)$	4.4×10^3	1	4.4×10^3
$e^-\gamma \to \nu q\bar{q}(\times 2)$	2.5×10^4	0.75	1.9×10^4
$e^-\gamma \to e^- q\bar{q}(\times 2)$	8.7×10^4	0.75	6.5×10^4

per fb^{-1}. The number of muons in the range of 50 to 100 GeV is about 1×10^4. Figure 9(b) shows the angular distribution of the muons. The number of tracks in the central region is about 8×10^3 per bin of 1°; it is significantly higher in the forward region. The total number of muon tracks available at the end of the first year is about 20×10^6 and 100×10^6 at the end of the second year.

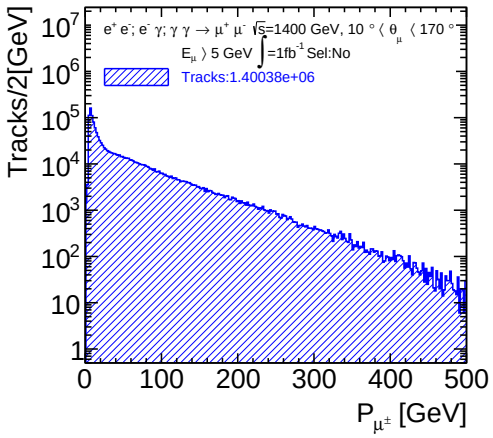

(a) muon momentum distribution

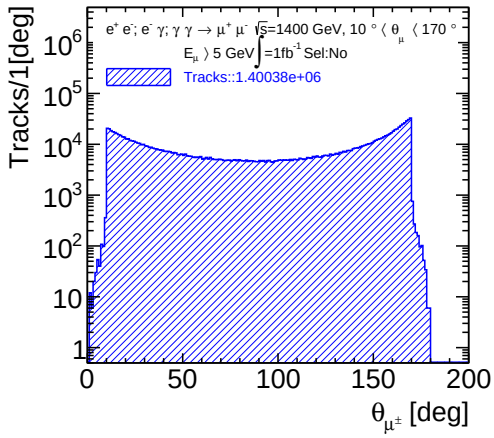

(b) muon angular distribution

Figure 9: $e^+e^-, e^-\gamma$ and $\gamma\gamma$ interactions with muon final states at $\sqrt{s}$=1400 GeV (a) muon momentum distribution (b) muon angular distribution

6.2 Momentum Resolution and Momentum Scale Calibration

At 1.4 TeV the cross section of the process $e^+e^- \to \mu^+\mu^-\gamma$ is small. As during the first two years the luminosity is small the $Z \to \mu^+\mu^-$ yield does not allow an accurate determination of the momentum scale using the di-muon mass. The measurement of the charged particle momentum scale is done measuring the $\pi^+\pi^-$ invariant mass of $K^0_s \to \pi^+\pi^-$ events. Figure 10(a) shows the hadron momentum distribution of the charged hadrons in the process $e^+e^-; e^-\gamma \to q\bar{q}$. Figure 10(b) shows the fit of the $\pi^+\pi^-$ invariant mass in the K^0_s region. The number of events in the plots correspond to an integrated luminosity of 1 fb^{-1}. $M_{K^0_s}$=0.4977 $\pm$ 2×10^{-5} GeV; the relative uncertainty on the global momentum scale is $\delta(M_{K^0_s})/M_{K^0_s}$=$4 \times 10^{-5}$. After the first year the high rate of K^0_s allows an accurate determination of the momentum scale as a function of the polar angle.

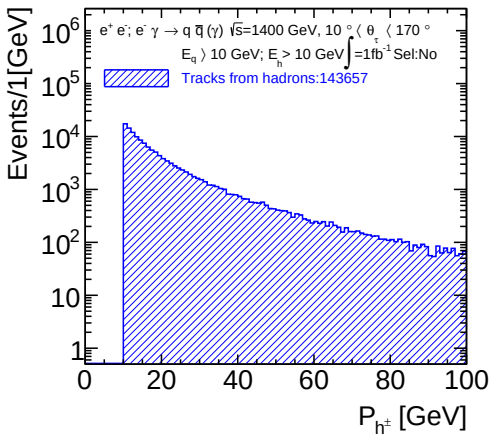

(a) h^+h^- momentum distribution

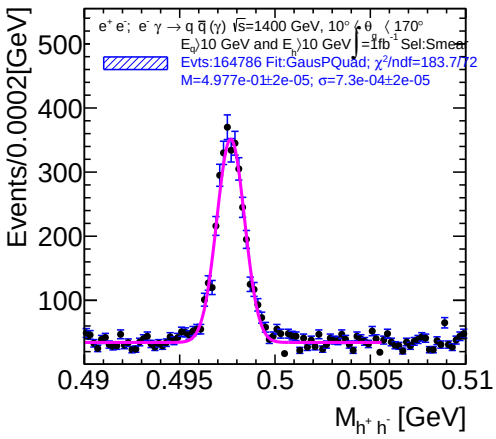

(b) h^+h^- invariant mass distribution

Figure 10: $e^+e^-;e^-\gamma \to q\bar{q}(\gamma)$ at $\sqrt{s}$=1400 GeV (a) h^+h^- momentum distribution (a) h^+h^- invariant mass distribution fit

6.3 Di-jet Energy Resolution and Energy Scale

Figure 11(a) shows the correlation between the di-quark invariant mass and the angle between the quarks for the processes $e^+e^-;e^-\gamma \to q\bar{q}\gamma$ at $\sqrt{s}$=1400 GeV; the di-quark angle ranges from 20° to 170°. Figure 11(b) shows the di-quark invariant mass; W events are clearly visible; a smaller Z peak is also visible. Figure 12(a) shows the di-jet invariant mass after quark fragmentation and hadronization and without particle energy smearing; the Fastjet exclusive kt algorithm is used for jet clustering. The W peak width is due to the jet confusion created by the small angle between the jets. Figure 12(b) shows the di-jet invariant mass after quark fragmentation and hadronization, and particle energy smearing. The W peak width is further increased by the particle energy resolution.

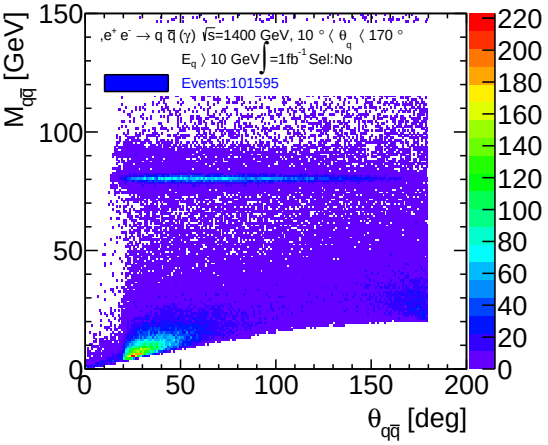

(a) Correlation between the di-quark invariant mass and the angle between the quarks

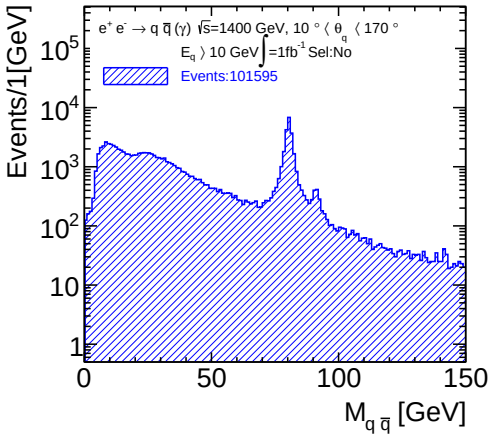

(b) di-quark invariant mass distribution

Figure 11: $e^+e^-;e^-\gamma \to q\bar{q}(\gamma)$ at $\sqrt{s}$=1400 GeV (a) Correlation between the di-quark invariant mass and the angle between the quarks (b) di-quark invariant mass distribution

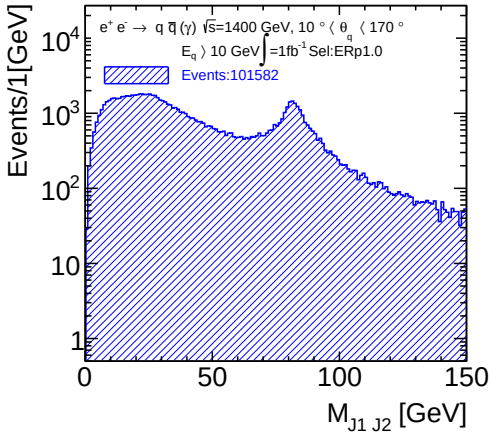

(a) di-jet invariant mass spectrum after jet clustering and without particle smearing

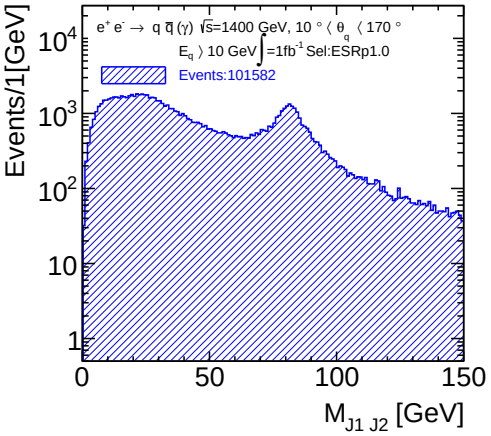

(b) di-jet invariant mass spectrum after jet clustering and particle smearing

Figure 12: $e^+e^-;e^-\gamma \to q\bar{q}(\gamma)$ at $\sqrt{s}$=1400 GeV (a) di-jet invariant mass spectrum after jet clustering and without particle smearing (b) di-jet invariant mass spectrum after jet clustering and with particle smearing

Figure 13(a) shows the di-jet invariant mass fit in the W, Z region; The Z peak is not visible. The fit result is M_W=81.41 $\pm$ 0.08 GeV and Γ_W=9.6 GeV. Figure 13(b) shows the di-jet invariant mass fit when rejecting Z events The fit result is M_W=81.28 $\pm$ 0.07 GeV and Γ_W=11.2 GeV. Even after rejection of $Z \to q\bar{q}$ events there is a shift in W mass due to the strong jet confusion.

At $\sqrt{s}$=1.4 TeV the poor di-jet mass resolution does not allow an accurate determination of the di-jet energy scale. The Z production rate is small and the jet confusion does not allow identifying Z events; the heavy flavour tagging efficiency measurement is an issue.

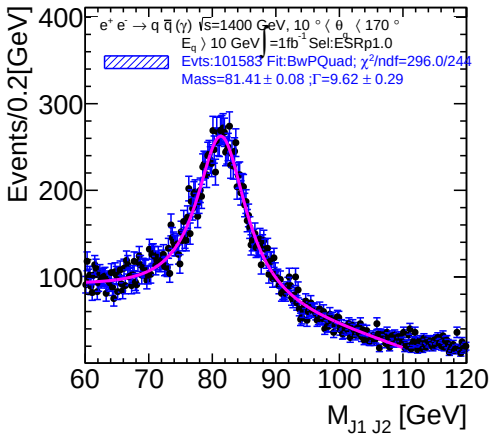

(a) di-jet invariant mass spectrum; all events

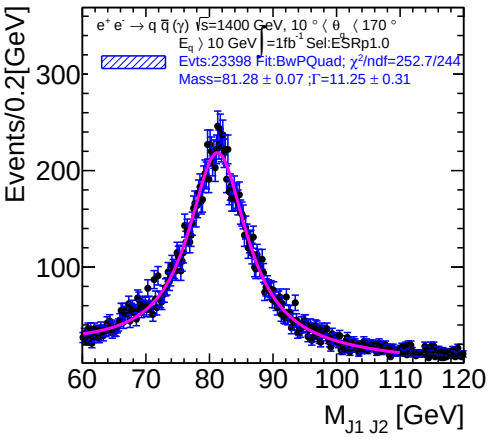

(b) di-jet invariant mass spectrum; no Z contribution

Figure 13: $e^+e^-;e^-\gamma \to q\bar{q}(\gamma)$ at $\sqrt{s}$=1400 GeV (a) di-jet invariant mass spectrum fit; all events (b) di-jet invariant mass spectrum fit; no Z contribution

7 Detector Calibrations at $\sqrt{s} = 91.2$ GeV

Table 8 shows the cross sections for $\mu^{\pm}$ and $q\bar{q}$ final states at $\sqrt{s} = 91.2$ GeV; it shows also the event rates assuming an integrated luminosity of 1 pb^{-1}.

Table 8: Di-muon and di-jet final state cross sections and event rates at $\sqrt{s}$=91.2 GeV

Process	Cross section [fb]	Events/pb^{-1}
	$E_f > 10$ GeV and $10^\circ < \theta_f < 170^\circ$	
$e^+e^- \to \mu^+\mu^-(\gamma)$	1.47×10^6	1.5×10^3
$e^+e^- \to q\,\bar{q}(\gamma)$	29.6×10^6	3×10^4

7.1 Momentum Resolution and Scale

Table 1 shows that in the first year of CLIC, the luminosity at $\sqrt{s}$=91.2 GeV is only 1 pb$^-$1 per day. In the second year the expected luminosity is 5 pb$^-$1 per day providing significant event samples for calibration. Figure 14(a) shows the muon momentum distribution (blue) of the process $e^+e^- \to \mu^+\mu^-$ after smearing. The red distribution shows the muon momentum distribution before smearing and with a scaling factor; the tail towards lower momenta is coming from events with ISR photons or with FSR photons. The distribution is peaked at 45.6 GeV. The figure shows also the fit result; $< P_\mu >$=45.56 $\pm$ 0.006 GeV; $\sigma(P)$=0.13 GeV. For muons of 45 GeV the momentum resolution is dominated by the contribution of the multiple scattering; $\sigma(P)/P = 2.6 \times 10^{-3}$ The relative accuracy on the momentum scale is $\delta(P)/P$=7×10^{-5}. Figure 14(b) shows the $\mu^+\mu^-$ invariant mass distribution (blue). The red distribution shows the true $\sqrt{s}$ distribution; the tail towards low values is coming from events with ISR photons. The fit result is M_Z=91.11 $\pm$ 0.01 GeV and $\sigma(M_Z)$=0.20 $\pm$ 0.014 GeV. At $\sqrt{s}$=91.2 GeV there is little background and the di-muon event sample provides a direct measurement of the momentum resolution at 45.6 GeV as well an and accurate determination of the momentum scale with a minimum dependence on the Monte Carlo.

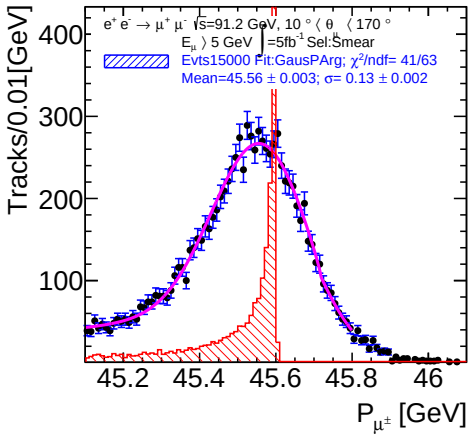

(a) $\mu^+\mu^-$ momentum distribution

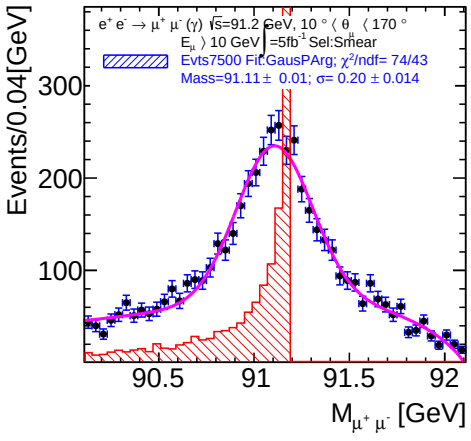

(b) $\mu^+\mu^-$ invariant mass distribution

Figure 14: $e^+e^- \to \mu\mu$ at $\sqrt{s}$=91.1 GeV (a) $\mu^+\mu^-$ momentum distribution (b) $\mu^+\mu^-$ invariant mass distribution

7.2 Di-jet Energy Resolution and Total Energy Scale

Figure 15(a) shows the di-jet total energy (blue) for events having the two quarks in the barrel region. To avoid any bias the di-jet energy is measured without jet clustering. The red distribution shows the true $\sqrt{s}$ distribution; the tail towards low values is coming from events with ISR photons. The energy distribution is very narrow; in production mode one measures directly the di-jet energy resolution; there is no contribution from the natural Z width. The fit result is $< E_{tot} >$=90.57 $\pm$ 0.016 GeV; $\sigma(E_{tot})$=1.52 $\pm$ 0.03 GeV. $\sigma(E_{tot})/E_{tot}$=1.7% ; it leads to $\sigma(E_{Jet})/E_{Jet}$=2.4%. The expected value using full simulation is 3.7% [9].

Figure 15(b) shows the di-jet total energy for events having the two quarks in the end-cap region. For this sample there is an increase of the width of the energy distribution because some particles from the jets escape detection when the polar angle is below 7°.

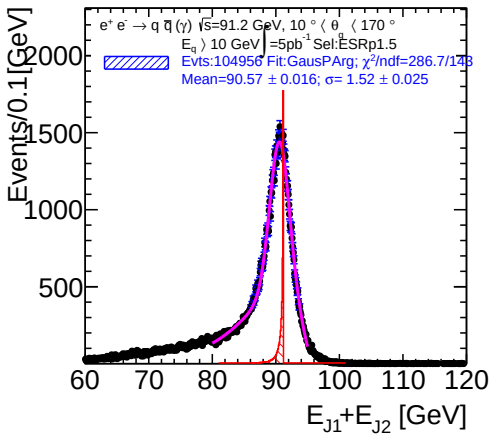

(a) Total energy distribution in barrel

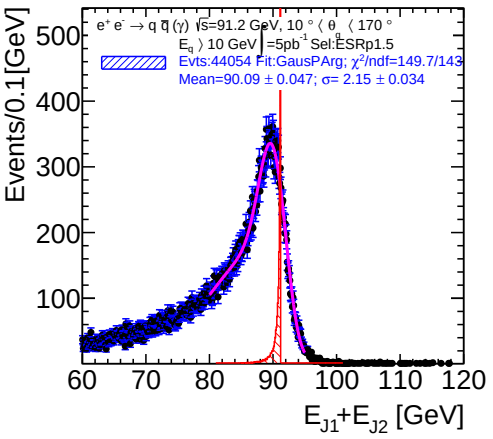

(b) Total energy distribution in end cap

Figure 15: $e^+e^- \to q\bar{q}(\gamma)$ at $\sqrt{s}$=91.2 GeV (a) Total energy distribution in barrel (b) Total energy distribution in end cap

The di-jet event sample provides also a significant amount of data to measure the heavy flavour tagging efficiency.

8 Summary

At $\sqrt{s} = 350$ GeV and 1.4 TeV the detector alignment can be done using $e^+e^-, e^-\gamma$ and $\gamma\gamma$ interactions with muon final states. At $\sqrt{s} = 350$ GeV the total rate is about 4×10^6 muon tracks at the end of the first year. At $\sqrt{s} = 1400$ GeV the total rate is about 20×10^6 muon tracks at the end of the first year. After the first year of running the high muon rate allows an accurate alignment and a regular control of the alignment parameters.

At $\sqrt{s}$=350 GeV, $Z \to \mu^+\mu^-$ and $K^0_s \to \pi^+\pi^-$ events allow a good control of the momentum resolution and an accurate determination of the global and differential momentum scale.

The di-jet mass resolution is poor and doesn't allow an accurate determination of the di-jet energy scale. The contamination of Z events by W's provides a data sample which requires Monte Carlo corrections for heavy flavour tagging efficiency measurement. Heavy flavour tagging efficiency measurement can also be done using $e^+e^- \to ZZ \to l^+l^-q\bar{q}$ events; it is only after the second year that the event rate is large enough.

At 1.4 TeV the cross section of the process $e^+e^- \to \mu^+\mu^-\gamma$ is small. As during the first two years the luminosity is also small the $Z \to \mu^+\mu^-$ yield does not allow an accurate determination of the momentum scale using the di-muon mass. The measurement of the charged particle momentum scale is done measuring the $\pi^+\pi^-$ invariant mass of $K^0_s \to \pi^+\pi^-$ events. Most di-jet events originate from W's; the poor di-jet mass resolution doesn't allow an accurate determination of the di-jet energy scale. The Z production rate is small and the jet confusion doesn't allow identifying Z events; the heavy flavour tagging efficiency measurement is an issue.

At $\sqrt{s}$=91.2 GeV there is little background; the di-muon event sample provides a direct measurement of the momentum resolution at 45.6 GeV and an accurate determination of the momentum scale. The di-jet event sample allows a direct measurement of the di-jet energy resolution and an accurate determination of the di-jet energy scale. It allows also the flavour tagging efficiency measurement

The back to back topology allows also a detailed check of the detector hermiticity. During the first stage of CLIC and after the first year, running at $\sqrt{s}$=91.2 GeV provides unique calibration features and an excellent opportunity to optimize the detector performance.

Several contributions to the total energy resolution cannot be approximated in a fast simulation. To characterize more accurately the jet energy calibration potential at $\sqrt{s}$=91.2 GeV requires full simulation and reconstruction.

9 Remaining Issues

Tracking systems alignment prior to the physics run?
Heavy flavour tagging efficiency measurement at $\sqrt{s}$=1.4 TeV.

10 Acknowledgments

We are grateful to Daniel Schulte for making available the ee, $\gamma\gamma$ and e γ beam spectrum at the various $\sqrt{s}$ energies and to all the colleagues who contributed to this study.

References

[1] L. Linssen et al., eds., *CLIC Conceptual Design Report: Physics and Detectors at CLIC*, CERN-2012-003, CERN, 2012, arXiv: 1202.5940 [physics.ins-det].

[2] D. Schulte, *Private Communication*, CERN.

[3] R. W. Assmann, *LEP Luminosity Revisited: Design and Reality*, proceedings of the Second Asian Particle Conference, Beijing, China, 2001.

[4] J. R. W. Kilian T. Ohl, *WHIZARD: Simulating Multi-Particle Processes at LHC and ILC*, Eur.Phys.J. **C71** (2011) 1742, DOI: arXiv:0708.4233[hep-ph].

[5] D. Schulte, *Beam-beam simulations with GUINEA-PIG*, CERN-PS-99-014-LP, CERN, 1999.

[6] S. M. T. Sjostrand, P. Z. Skands, *PYTHIA 6.4 Physics and Manual*, JHEP **05** (2006), DOI: hep-ph/0603175.

[7] M. Cacciari, G. P. Salam, *Dispelling the N^3 myth for the k_t jet-finder*, Phys. Lett. **B641** (2006), DOI: hep-ph/0512210.

[8] C. Collaboration, *Alignment of the CMS tracker with LHC and cosmic ray data*, Journal of Instrumentation (2014), DOI: arXiv:1403.2286V2[physics-ins-det].

[9] M. A. Thomson, *Particle Flow Calorimetry and the PandoraPFA Algorithm*, Nucl. Instrum. Methods. **A611** (2009) 25, DOI: arXiv:0907.3577.